Stierle, E., Bohnhoff, M., Vavrycuk, V. (2014): Resolution of non-double-couple components in the seismic moment tensor using regional networks-II: application to aftershocks of the 1999 Mw 7.4 Izmit earthquake. - Geophysical Journal International, 196, 3, pp. 1878—1888.

DOI: http://doi.org/10.1093/gji/ggt503

Geophysical Journal International

Geophys. J. Int. (2014) **196,** 1878–1888
Advance Access publication 2014 January 13

doi: 10.1093/gji/ggt503

Resolution of non-double-couple components in the seismic moment tensor using regional networks—II: application to aftershocks of the 1999 M_w 7.4 Izmit earthquake

Eva Stierle,[1] Marco Bohnhoff[1,2] and Václav Vavryčuk[3]

[1] *Helmholtz-Centre, Potsdam German Research Centre for Geosciences (GFZ), Telegrafenberg, D-14473 Potsdam, Germany. E-mail: stierle@gfz-potsdam.de*
[2] *Department of Earth Sciences, Free University Berlin, Malteser Strasse 74-100, D-12249 Berlin, Germany*
[3] *Institute of Geophysics, Academy of Sciences of the Czech Republic, Boční II/1401, CZ-14131 Prague, Czech Republic*

Accepted 2013 December 10. Received 2013 December 10; in original form 2013 April 10

SUMMARY

We study potential non-double-couple (non-DC) components in aftershocks of the 1999 Izmit earthquake. The Izmit earthquake ruptured a ∼140-km-long segment of the North Anatolian Fault Zone in northwestern Turkey and was followed by the $M_w = 7.1$ Düzce earthquake that extended the rupture further to the east. Focal mechanisms of Izmit aftershocks clearly indicate a segmentation of the rupture into several segments, one of which is the Akyazi Plain, a pull-apart structure, where significant non-DC components might be observed. The analysed earthquake catalogue contains waveforms of more than 4000 accurately located events observed at 35 three-component short-period seismic stations. To ensure high-quality data with good focal coverage, we apply strict quality criteria to the aftershock catalogue reducing the number of events to only 33 aftershocks for which stable moment tensors were calculated using *P*- and *S*-wave amplitudes. The moment tensors of the 33 analysed aftershocks display significant differences in the percentage of the non-DC components for the three distinct fault segments: the Izmit-Sapanca, Karadere-Düzce and the Akyazi segments. Events located in the Izmit-Sapanca and Karadere-Düzce segments exhibit only small percentages of the non-DC components and if existent they are mainly positive. This correlates well with the predominant strike-slip stress regime along these segment and also with the main shock rupture being right-lateral strike-slip. In contrary, we found a substantial percentage of non-DC components for events below the Akyazi Plain where the Sapanca Fault splits into the Mudurnu and Karadere faults. There, the observed non-DC components are entirely positive indicating a tensional regime and ranging from 20 to 48 per cent, clearly exceeding the defined error bounds found in a synthetic study. This observation is in accordance with the post-seismic setting following the Izmit main shock that left a remarkable slip deficit of 3.5 m below the Akyazi bend.

Key words: Earthquake source observations; Seismicity and tectonics; Continental tectonics: extensional.

GJI Seismology

1 INTRODUCTION

The seismic moment tensor has become one of the most efficient tools for describing and investigating earthquake source processes. It contains information on the orientation of a fault, slip direction and type of faulting. It is capable to describe shear faulting on a planar rupture surface by its double-couple (DC) component but it may reveal also deviations from pure shear faulting if non-double-couple (non-DC) components are present in the moment tensor (Julian *et al*. 1998; Miller *et al*. 1998). The origin of non-DC components can be either in the source process itself ('real' non-DC) reflecting specific physical properties of the source (Foulger *et al*. 2004) or in the medium in the focal area (Vavryčuk 2005). Furthermore, non-DC components can be artefacts of data processing ('artificial' or 'spurious' non-DC components) produced by errors in the velocity structure, hypocentre location or noise in the data (Šílený 2009). The most common origins of the real non-DC components are: (1) volumetric changes in the source area resulting in tensile faulting with crustal fluids playing an important role (Vavryčuk 2002) or (2) a complex fault geometry (e.g. Julian *et al*. 1998).

Here, we focus on detecting potential non-DC components in aftershocks of the 1999 $M_w = 7.4$ Izmit. The Izmit earthquake ruptured a ∼140-km-long segment of the North Anatolian Fault Zone (NAFZ) in northwestern Turkey and it was followed by another main shock, the $M_w = 7.1$ Düzce earthquake, 3 months later extending the rupture further to the east (e.g. Tibi *et al*. 2001; Gülen *et al*. 2002).

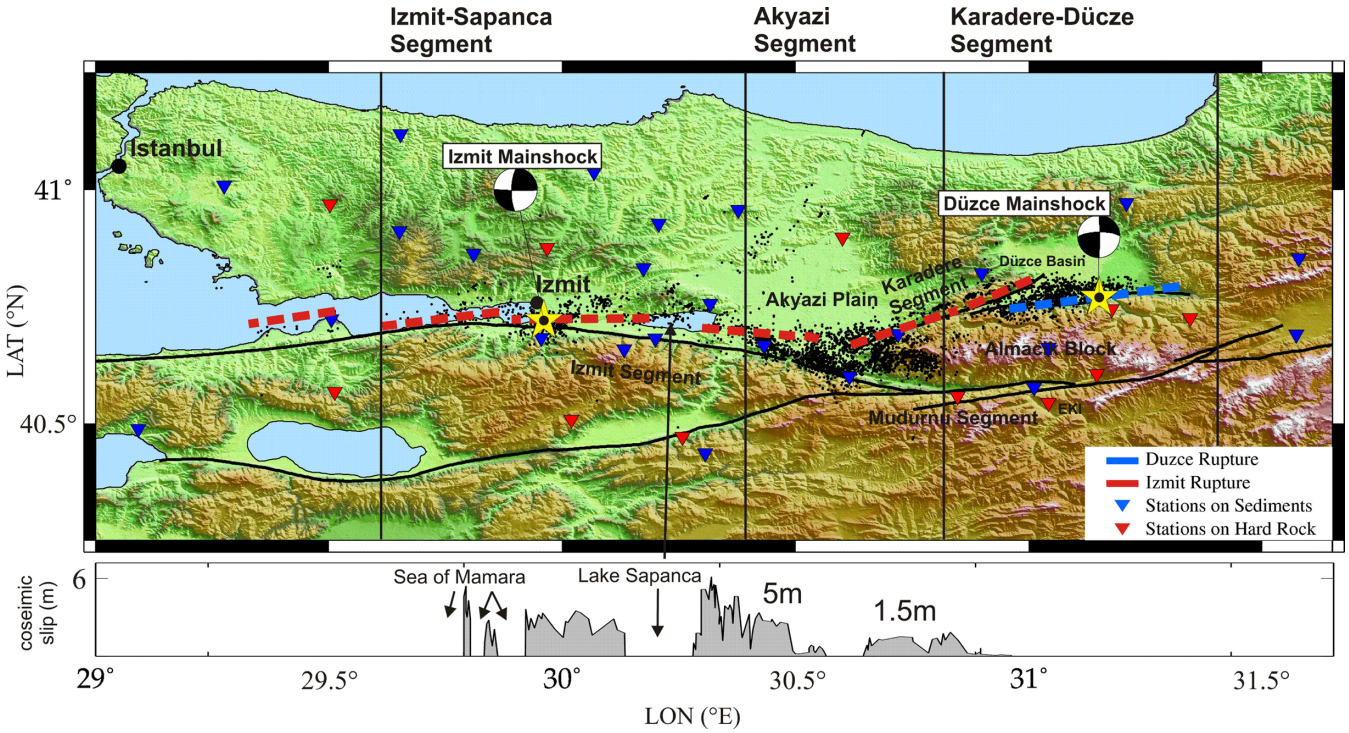

Figure 1. Seismotectonic setting of the Izmit section of the North Anatolian Fault Zone (NAFZ) with major mapped faults and surface ruptures of the 1999 Izmit and subsequent Düzce earthquakes (after Barka *et al*. 2002). Black dots represent relocated aftershocks from Bulut *et al*. (2007) and triangles denote locations of stations. The segmentation along the Izmit rupture is based on lateral changes of aftershock focal mechanisms (after Bohnhoff *et al*. 2006). Fault lines are taken from the Turkey General Directorate of Mineral Research and Exploration. Lower plot: lateral distribution of coseismic surface slip during the Izmit earthquake (after Barka *et al*. 2002).

A 35-station seismic network covering the entire Izmit rupture with an average spacing of about 15 km was completed only 4 d after the main shock allowing to record a unique data set of Izmit aftershocks (Baumbach *et al*. 2003; Bulut *et al*. 2007; Fig. 1). Analysis of Izmit aftershock focal mechanisms allowed to identify a strong partitioning of deformation and stress along the rupture (Bohnhoff *et al*. 2006). While focal mechanisms of the Izmit and subsequent Düzce main shock indicate right-lateral strike-slip faulting, about 40 per cent of all Izmit aftershock focal mechanisms were EW-extensional normal faulting, pinpointing to an extensional structure below the Akyazi Plain (Akyazi Segment in Fig. 1). This area reflects a local topographical depression subsided by ∼500 m with respect to the surrounding region representing a small pull-apart structure similar to the Sea of Marmara (Armijo *et al*. 2002) but in a more juvenile state (Bohnhoff *et al*. 2006). The occurrence of normal faulting mechanisms below the Akyazi Plain is well explained by the coseismic slip deficit of ∼3.5 m (Tibi *et al*. 2001; Barka *et al*. 2002). The slip deficit activated pre-existing NS-oriented normal faults (Bulut *et al*. 2007) suggesting strong tensional components, which is abetting the occurrence of non-DC components of moment tensors. Therefore, we selected the Izmit rupture as an ideal site to study the occurrence of non-DC components in aftershock moment tensors during a post-seismic scenario. For a comparison, we also include the Izmit-Sapanca and Karadere-Düzce segments of the Izmit rupture where dominantly strike-slip mechanisms are observed (Fig. 1).

Note that reliably detecting potential non-DC components in moment tensors is not an easy task but a rather demanding procedure which needs: high-quality data observed by a dense network of stations, accurate locations and good knowledge of the medium. Obviously, in most cases, it is not possible to fully satisfy such strict criteria and thus to completely exclude the presence of spurious non-DC components. Therefore, any proper analysis of observed non-DC components should include a resolution study revealing detection capability of the given network. Such a study for the Izmit aftershocks is presented in the companion paper by Stierle *et al*. (2014). This paper shows that the given regional network configuration is, in principal, capable to detect the real non-DC components provided, if (1) the real non-DC components are higher than ±15 per cent, (2) the moment tensors are inverted using *P*- as well as *S*-wave amplitudes, (3) absolute errors in hypocentre location are smaller than 2.5 km (Bulut *et al*. 2007) and (4) at least basic characteristics of the velocity model are known when computing the Green's functions (e.g. whether the analysed station is deployed on the sediments or hard rock). The synthetic study also reveals that the retrieved isotropic (ISO) percentage is more reliable than the compensated linear vector dipole (CLVD) percentage and that the constrained moment tensor inversion for a shear-tensile model is preferable over the full moment tensor inversion with no constraints.

2 DATA AND METHOD

Aftershocks of the 1999 Izmit earthquake were recorded by a 35-station seismic network covering the entire rupture zone. Stations were equipped with three-component sensors of 1 Hz natural frequency. Waveform recordings are simple and generally show good signal-to-noise ratios with clear *P*- and *S*-wave onsets (Fig. 2). The seismograms are sufficiently broad-band for local events with magnitudes between 1 and 4, so they do not need to be corrected for the instrument response. Waveforms of events with a greater magnitude (>4) might by distorted in the low frequency range and the

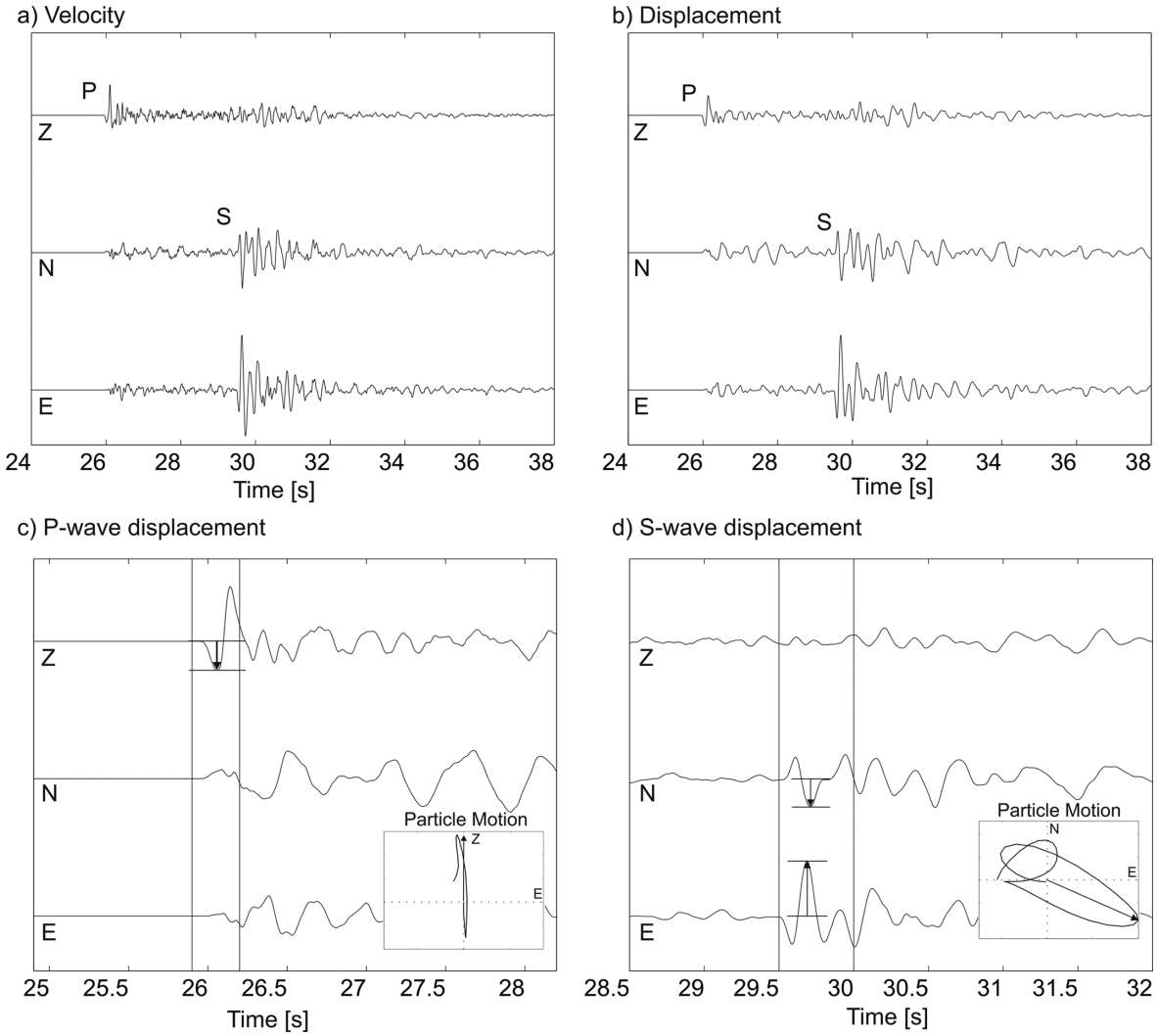

Figure 2. Velocity and displacement recordings of $M_w = 3.4$ 1999 Izmit aftershock (Event ID 28) recorded at station EKI (Fig. 1) and located at an epicentral distance of 27 km. (a) Velocity recordings. (b) Displacement recordings, filtered with a bandpass filter between 0.5 and 35 Hz. (c) and (d) *P*- and *S*-wave displacement, respectively. Black lines denote the time frame used for the particle motion plot indicating the direction of the incoming *P* and *S* waves, respectively.

scalar seismic moment can be underestimated. Since waveforms at all stations are distorted in the same way, the absolute values of the moment tensors are affected, but the relative values of the moment tensors should remain correct. Since we invert only for the relative moment tensors, our results are not affected by the instrument response. The network recorded more than 10 000 events of which 4600 events were relocated with an internal precision of less than 400 m. The aftershocks delineate the entire rupture zone and focal depth extends down to 16 km (Bulut *et al*. 2007).

Strict selection criteria are needed to fulfil requirements for reliable characterization of potential non-DC components in the moment tensors Stierle *et al.* (2014). To ensure high-quality data, we selected events by applying the following criteria: (1) The event was recorded at a minimum of 15 stations; (2) The magnitude of the events must fall in the range between 2 and 4.5 and (3) The hypocentral depth is between 5 and 16 km. Applying these constraints to the catalogue of located aftershocks, the number of events decreased from 4500 to 667. Of these, 140 were located along the Izmit-Sapanca Segment, 368 along the Akyazi Segment and 159 along the Karadere-Düzce Segment, respectively (see Fig. 1).

The *P*- and *S*-wave amplitudes were measured on the displacement records filtered with a Butterworth bandpass filter with corner frequencies 0.5 and 35 Hz to reduce noise effects. Since the incidence angle of arriving waves is near vertical at most stations because of the uppermost soft-sedimentary layer, we picked the *P*-wave amplitudes on the vertical components and the *S*-wave amplitudes on the horizontal components, respectively (Fig. 2). The amplitudes were picked manually, where the maximum *S*-wave amplitudes were further constrained by visual inspection of particle motion plots (Fig. 2). Since the *S* waves were usually more complicated and difficult to interpret, we measured only clear *S*-wave amplitudes mostly from stations with small epicentral distances. Measurements of the *S* waves which displayed any anomalies such as shear wave splitting (Hurd & Bohnhoff 2012; Eken *et al*. 2013) were excluded. As a result, we were able to include up to six *S*-wave amplitudes per event. Nevertheless, information on the *S*-wave amplitudes was important in the inversion and considerably stabilized the resultant moment tensors (see Stierle *et al.* 2014).

The Green's functions are determined using ray theory (Červený 2001). Since the modelling of P_n waves is complicated and cannot

Table 1. 1-D velocity models of the crust. v_P is the *P*-wave velocity (modified after Bulut *et al*. 2007), v_P/v_S is the ratio of *P*- and *S*-wave velocities, Q_P and Q_S are the quality factors of *P* and *S* waves, respectively.

v_P (km s^{-1})	Depth (km)	v_P/v_S	Q_P	Q_S
(a) Stations on sediments				
2.90	0.00	1.75	150	75
4.70	1.00	1.75	400	200
5.30	7.00	1.75	550	275
6.06	11.00	1.75	700	350
7.20	15.00	1.75	800	400
8.06	35.00	1.75	1000	500
(b) Stations on hard rock				
4.70	0.00	1.75	400	200
5.30	7.00	1.75	550	275
6.06	11.00	1.75	700	350
7.20	15.00	1.75	800	400
8.06	35.00	1.75	1000	500

easily be calculated with standard ray theory, recordings for epicentral distances larger than 80 km were excluded. The effect of the flat free Earth's surface is incorporated in the Green's functions. As in Stierle *et al.* (2014), we used two smoothed velocity models (Table 1) in order to be able to distinguish between stations on hard rock and stations on a shallow sediment layer. Stations on hard rock are defined as suggested by Parolai *et al*. (2004). The remaining stations are considered to be situated on sediments. Since attenuation is different for hard rock and sediments (Bindi *et al.* 2006) we corrected theoretical amplitudes for the effect of attenuation after Červený (2001) using a dissipative filter, which yields the frequency-dependent traveltime perturbations along rays. The attenuation parameters Q_P and Q_S are listed in Table 1. We tested also some other values of attenuation and evaluated errors due to an inaccurate attenuation model and found that these errors are insignificant.

We started with inverting the *P*- and *S*-wave amplitudes for the full moment tensors using a linear inversion scheme. Results are shown in Table 2. We found that the moment tensors display a rather high scatter, in particular, in the CLVD component, which was about three times larger than in the ISO component. To stabilize the inversion, we decided to invert for the shear-tensile source model using a non-linear inversion as described in Stierle *et al.* (2014). Before applying this constrained inversion, we tested whether the shear-tensile source model is consistent with the data and thus suitable for the data interpretation. According to Vavryčuk (2011, eq. 21), we determined the consistency coefficient for the analysed events. The coefficient can range from −1 to 1; positive values indicate that the data are consistent with the shear-tensile model, and negative values are a measure of the inconsistency. The closer the value is to −1 the stronger is the inconsistency. We

Table 2. Focal mechanisms and non-DC components obtained by the full moment tensor inversion, and their consistency factor determined after Vavryčuk (2011) for 33 selected events.

ID	Strike	Dip	Rake	DC (per cent)	CLVD (per cent)	ISO (per cent)	Consistency factor
1	80.1	61.4	124.0	48	31	20	0.5
2	136.2	79.4	−12.1	88	−2	11	−0.1
3	328.4	78.7	20.2	66	22	12	0.3
4	242.0	74.1	−139.9	58	38	4	0.4
5	149.1	79.0	7.3	61	39	0	0.4
6	80.0	68.6	168.8	96	−4	0	0.0
7	351.4	45.2	−35.6	83	16	−1	−0.2
8	207.5	76.4	−168.5	56	43	2	0.4
9	262.7	67.8	−72.3	72	23	5	0.3
10	201.6	58.2	−36.9	75	−7	17	−0.2
11	348.4	50.9	−139.1	79	0	20	0.2
12	335.3	55.1	−149.8	77	−1	22	−0.2
13	355.4	48.8	−102.9	66	16	18	0.3
14	191.4	43.1	−88.1	89	−9	2	−0.1
15	187.8	66.4	−66.7	80	2	18	0.2
16	329.0	60.0	−144.0	51	8	41	0.5
17	335.2	65.2	−139.4	23	45	32	0.8
18	8.1	44.1	−79.3	54	24	22	0.5
19	230.8	59.8	−53.9	66	16	18	0.3
20	161.6	44.0	−148.1	80	−6	14	−0.2
21	136.7	69.6	115.9	24	44	33	0.8
22	201.2	33.0	−33.6	76	16	7	0.2
23	1.6	48.5	−109.4	76	15	9	0.2
24	224.8	67.5	−47.4	66	−13	21	−0.3
25	143.8	85.1	146.9	57	13	30	0.4
26	181.5	49.3	43.1	80	6	14	0.2
27	80.3	85.1	157.3	66	−23	11	−0.3
28	300.5	77.7	141.9	75	−16	8	−0.2
29	175.6	88.7	−14.6	84	9	7	0.2
30	12.3	88.4	−5.1	42	57	2	0.6
31	156.1	76.6	6.6	73	13	14	0.3
32	243.7	64.3	138.5	29	53	17	0.7
33	153.6	86.3	−6.6	70	−16	14	−0.3

obtained values between −0.3 and 0.8, where the most events yield positive consistency factors (Table 2). This indicates that the shear-tensile source model is appropriate to be adopted in the inversion. A detailed description of individual steps of the inversion constrained to a shear-tensile source model can be found in Stierle *et al.* (2014).

The decomposition of the moment tensor into the percentages of DC and non-DC components was performed after Vavryčuk (2001), where the non-DC component consists of the ISO and CLVD components. The reliability of the moment tensor solution was assessed by the misfit of theoretical and observed amplitudes and by inverting data contaminated by random noise and by Jackknife tests. The misfit was calculated by the normalized root-mean-square (rms) difference between theoretical and observed amplitudes (Stierle *et al.* 2014, eq. 5).

Rms Values close to zero represent a good fit of amplitudes whereas rms values close to one indicate no fit of amplitudes. Solutions were classified as reliable if the misfit was smaller than 0.3. Furthermore, to assess the stability of the retrieved moment tensor, we repeated the inversion with randomly generated noisy input data as well as we inverted subsets of available data (Jackknife test). The noise is uniformly distributed with a maximum noise level reaching 25 per cent of the observed amplitude at the respective station. For each event, 100 realizations were performed. For the Jackknife test, we run several inversions in which one station was excluded. Thus the number of realizations equals the number of stations recording the respective event minus 1. The resulting errors in terms of standard deviations are similar to the errors obtained by noise tests. Fig. 3 shows the best-fitting moment tensor solution as well as the results for the noise test of one event in each segment using constrained and full moment tensor inversion techniques. The scatter of compressional (*P*) and tensional (*T*) axes and errors in the non-DC components are higher when using full moment tensor inversion. Thus, the constrained moment tensor inversion reveals much more stable results with smaller errors in the non-DC components, which is in a good correspondence with our observations in the synthetic case study (Stierle *et al.* 2014).

The large scatter of *P*- and *T*-axes of the retrieved moment tensors as well as high variations in non-DC components are indicators of unstable and thus unreliable mechanisms. We defined an event to be stable if the mean deviation of the *P*- and *T*-axes was less than 10° and if the standard deviation of the percentage for the ISO and CLVD components was less than ±15 per cent, respectively, according to the retrieved error bounds of Stierle *et al.* (2014). Furthermore, we also compared the moment tensor solution constrained to the shear-tensile source model to the solution of the full moment tensor inversion. For stable solutions, the *P*- and *T*-axes deviated with angles less than ±10°.

3 RESULTS AND DISCUSSION

We analysed 667 events from the Izmit aftershock catalogue fulfilling the constraints described earlier. Applying strict stability conditions to ensure only high-quality moment tensors, the number of events was further reduced to a total of 33. This decrease is drastic but well explained by applying profound quality criteria as pointed out above and based on the synthetic study for the Izmit aftershock network (Stierle *et al.* 2014). Note that a similar reduction of events was also reported for the study of non-DC components for induced seismic events at the Geysers geothermal field in California (Ross *et al*. 1996).

We found that including *S*-wave amplitudes in the moment tensor inversion is essential in most cases for stabilizing the moment tensors. Even including a few *S*-wave amplitudes was important and reduced errors in the non-DC components. Especially for rather poor focal sphere coverage, the inversion of *P*-wave amplitudes can be unstable and not reliable. Here, including the *S*-wave amplitudes is essential for improving the moment tensor solutions.

Of the 33 events, nine are located along the Izmit-Sapanca Segment, 17 along the Akyazi Segment and seven along the Karadere-Düzce Segment. The magnitudes of the events range from 2.5 to 4.3. The strike, dip and rake as well as the rms values of the analysed events are listed in Table 3; the retrieved non-DC contents of moment tensors are listed in Table 4. Furthermore, the standard deviations of the ISO and CLVD components are given as a result of the noise and Jackknife tests. We obtained misfits ranging from 0.04 to 0.28. Standard deviations of the ISO and CLVD components are similar for the noise and Jackknife test being up to ±9 per cent.

The full moment tensor solutions for all 33 stable events are plotted on the lower hemisphere in Fig. 4. Fig. 5 shows the epicentre locations of the events along the Izmit rupture together with the beach balls showing the full moment tensor solutions. Events along the Izmit-Sapanca Segment are predominantly strike-slip mechanisms being well represented by simple shear on a planar surface. Events 2, 3, 4, 5 and 8 are pure shear strike-slip mechanisms which occurred off the main fault with a strike rotated by about 40° on average with respect to the EW strike of the main fault. These events might indicate reactivation of secondary Riedel-type faults (Tchalenko 1970) developed in early stages of the evolution of the North Anatolian Fault and currently being located within a few kilometres to the principal slip zone to either side of the fault. This observation is in a good agreement with Izmit aftershocks being generally located off-fault (Bulut *et al*. 2007). For the remaining events along the Izmit-Sapanca Segment (some of them include substantial normal faulting components), one of the possible fault planes roughly follows the strike of the main fault. These results correspond with the transtensional tectonic setting at this part of the Izmit rupture (Bohnhoff *et al*. 2006).

Along the Akyazi Segment, we retrieved stable moment tensors of 17 events. Almost all events show pure EW-extensional normal faulting mechanisms with significant positive non-DC components. These events are located below the Akyazi Plain, an area of a local topographic depression subsided by 500 m with respect to the surrounding formations. In the Akyazi Plain north of the Izmit surface rupture, almost no aftershocks are observed since no strain was released here during the main shock. Towards the east, the main fault splits into the NE-trending Karadere Fault and the ESE-trending Mudurnu Segment. While the Karadere Fault was activated during the Izmit event the Mudurnu section that hosted an *M*7.1 earthquake in 1967 (Ambraseys & Zatopek 1969) remained inactive during the Izmit rupture and even did not host a single aftershock. This indicates that it is still early in its seismic cycle. The scatter of event locations below the Akyazi Plain as well as the fragmentation of the formation into several small-scale NS-trending faults (Bulut *et al*. 2007) indicates complex structures, where the released strain from the main shock is distributed over several subsidiary faults. Here, a significant slip deficit of approximately 3.5 m was accumulated during the Izmit main shock resulting in pronounced aftershock activity with predominantly EW-extensional normal faulting mechanisms (Bohnhoff *et al*. 2006) promoting tensional components in the source mechanism manifested by significant positive non-DC components. We identified only one event out of 17 events located along this segment reflecting a strike-slip mechanism (Event 26 in Tables 3 and 4). This pure shear event occurred 17 d after the main shock. Approximately 12–16 d after the main shock, when most

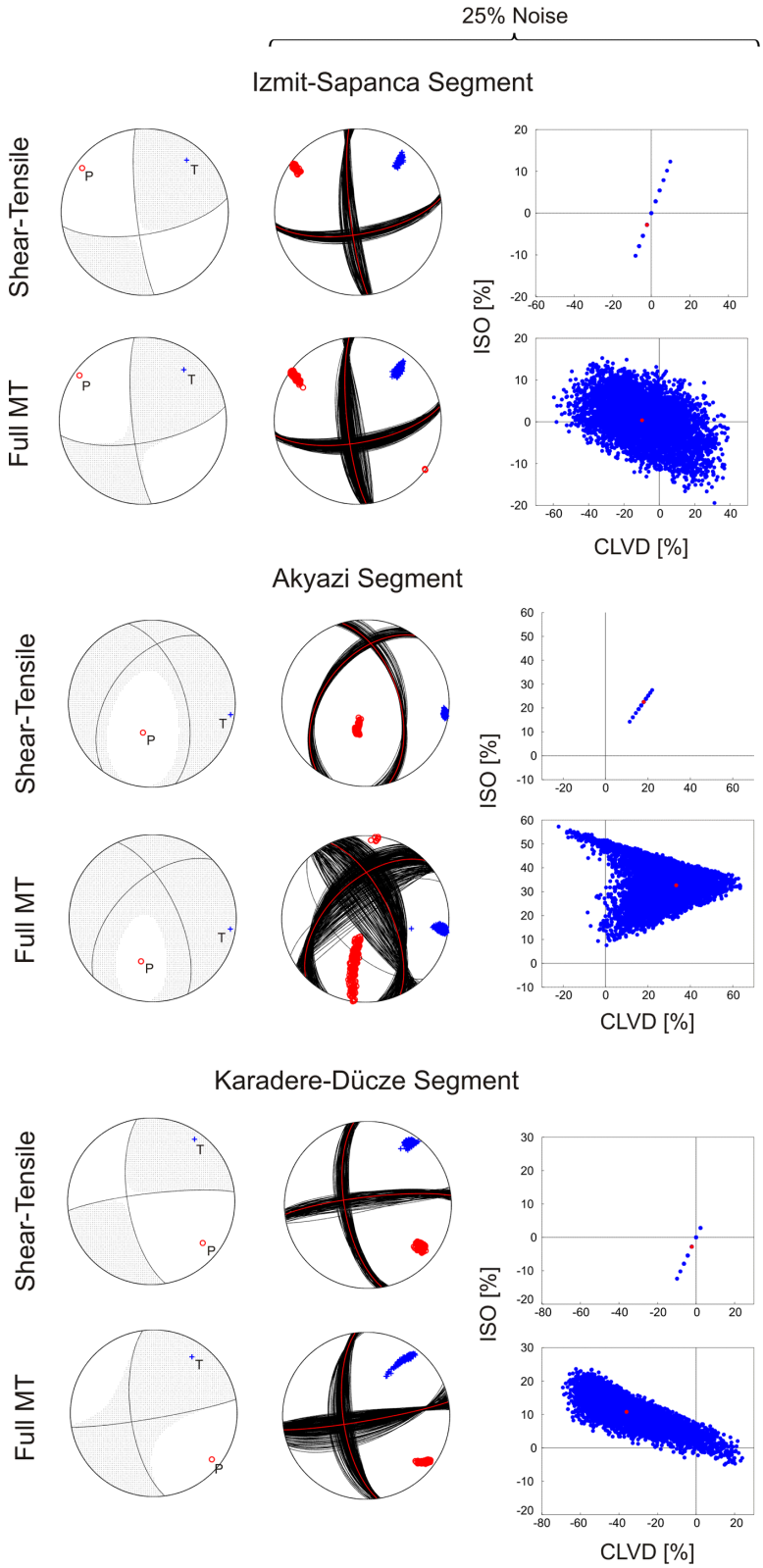

Figure 3. Results of the inversion for selected events from each of the three segments along the Izmit rupture (Izmit-Sapanca Segment: Event 6, Akyazi Segment: Event 17 and Karadere-Düzce Segment: Event 27). Stable results obtained by constrained (top row) and full (bottom row) moment tensor inversion are shown. Left-hand column shows the best-fitting solution, middle and right-hand columns show the scatter of nodal lines, *P*- and *T*-axes and distribution of non-DC components, respectively, computed by adding random noise with a level of 25 per cent to analysed amplitudes.

Table 3. Focal mechanisms in terms of strike, dip and rake of 33 selected events obtained by the inversion constrained to the shear-tensile source model. Furthermore, the origin time, local magnitude (M_L), number of *P*- and *S*-wave amplitudes inverted and the rms are shown.

ID	Month	Day	Hour	Min	Sec	Lat (°)	Lon (°)	Dep (km)	M_L	# *P* amp	# *S* amp	rms	Strike (°)	Dip (°)	Rake (°)
1	8	27	15	40	30.6	40.73	30.13	15.0	3.5	19	3	0.13	190	82	18
2	8	28	8	28	36	40.73	30.02	10.9	3.8	19	5	0.11	230	80	−162
3	9	2	19	33	33.2	40.74	30.02	10.0	2.8	18	3	0.12	327	88	14
4	9	4	10	31	43.3	40.73	30.01	9.8	4.3	18	5	0.20	141	63	−8
5	9	4	10	45	51	40.73	30.02	11.2	3.2	14	5	0.15	149	80	9
6	9	4	18	28	33.9	40.74	30.35	11.0	3.9	13	8	0.12	80	68	171
7	9	24	13	45	41.6	40.74	30.28	13.0	4.1	14	2	0.05	106	67	−131
8	10	5	4	10	53.8	40.77	29.85	9.6	3.7	16	2	0.23	204	71	−166
9	10	9	21	33	36.9	40.78	30.08	8.7	3.3	12	6	0.25	43	32	−130
10	8	30	4	1	2.4	40.64	30.54	11.1	2.7	19	3	0.28	201	57	−36
11	8	30	19	22	48.4	40.65	30.68	11.1	2.5	21	1	0.16	226	57	−52
12	9	1	2	54	31.1	40.66	30.71	11.1	2.6	21	1	0.16	220	63	−52
13	9	1	4	3	44.5	40.68	30.56	11.1	2.8	21	6	0.07	350	50	−110
14	9	1	19	9	27.9	40.64	30.63	10.5	2.5	17	5	0.18	191	43	−90
15	9	1	21	39	7.5	40.67	30.72	13.0	2.6	15	4	0.11	189	68	−65
16	9	3	14	23	24.5	40.66	30.62	11.1	2.9	19	1	0.14	350	47	−110
17	8	30	18	0	50.1	40.65	30.56	11.1	2.7	17	6	0.20	343	57	−126
18	9	2	18	39	41.2	40.67	30.62	11.1	3.1	16	2	0.28	6	45	−84
19	9	1	1	0	15.2	40.68	30.67	11.0	2.8	17	5	0.26	229	59	−57
20	9	2	11	19	4.3	40.65	30.67	10.9	3.3	16	7	0.24	163	43	−138
21	8	30	4	35	16	40.63	30.64	15.4	3.2	17	3	0.16	342	79	−112
22	9	1	17	15	29.1	40.68	30.45	11.3	2.6	20	3	0.24	196	32	−42
23	9	2	7	0	42.3	40.65	30.57	11.1	2.9	14	7	0.23	0	48	−111
24	9	2	7	10	15.6	40.66	30.68	10.9	2.8	15	4	0.28	220	70	−55
25	9	2	14	21	4.6	40.64	30.70	13.7	2.7	16	3	0.16	230	64	−20
26	9	3	7	26	53.6	40.66	30.58	11.1	2.8	18	4	0.26	68	68	140
27	8	30	0	57	3.3	40.80	31.06	7.0	3.1	16	1	0.09	263	82	−157
28	9	2	4	18	23.1	40.77	31.11	7.2	3.4	16	6	0.24	39	55	17
29	10	2	2	47	52.7	40.79	31.06	7.7	3.1	14	4	0.12	175	88	−18
30	9	1	7	58	1.8	40.74	30.97	7.0	3.0	14	2	0.18	190	89	10
31	10	13	11	11	36.2	40.78	30.96	7.0	3.4	12	3	0.04	155	89	−9
32	9	12	14	34	53.8	40.76	31.01	5.7	3.3	14	2	0.15	241	76	132
33	8	30	21	14	5.8	40.75	30.82	12.9	3.4	18	2	0.20	243	84	−176

of the 3.5 m slip deficit below the Akyazi Plain seemed to have been adjusted, the extensional normal faulting regime deceased and migrated towards the Düzce Basin where the Düzce event nucleated 87 d after the Izmit earthquake. The strike-slip event below the Akyazi Plain with insignificant non-DC components thus supports the findings that this part of the Izmit rupture released the coseismic slip deficit within the first 2 weeks after the main shock then turning back to its pre-Izmit strike-slip, pure shear setting (Ickrath *et al.* 2013).

East of the Akyazi Plain, we retrieved stable moment tensors for seven events that were located along the Karadere-Düzce Segment. Since this segment is situated at the eastern end of the network (and the Izmit rupture) the azimuthal coverage is rather poor compared to the remaining segments and therefore it was particularly difficult to obtain stable results despite the high number of aftershocks in this region. Fault plane solutions for these events are dominantly strike-slip, which is in agreement with the observations of Orgülü & Aktar (2001) and Görgün *et al*. (2010). The percentage of non-DC components is insignificant. Events 31 and 33 are located on the N65°-trending, steeply NW-ward dipping Karadere Fault and one of the nodal planes of both mechanisms matches well the trend and dip of the Karadere Fault. The strike of the events further to the east coincides with the trend of the Düzce Fault except for event 28 being inclined by approximately 30°. Seeber *et al*. (2000) observed that focal mechanisms in this area are highly diverse reflecting normal faulting as well as strike-slip mechanisms. They suggest that many of the aftershocks originate from secondary faults, straddling the volume between main strands. In our case, we did not observe any normal faulting or thrust event.

The seismic moment tensors of the 33 analysed events display significant differences in the percentage of the non-DC components for the three distinct fault segments (Fig. 6). Events located in the Izmit-Sapanca and Karadere-Düzce segments exhibit only small percentages of the non-DC components and if existent they are mainly positive. The non-DC components are generally smaller than 10 per cent except for events 32 and 29 located in the Karadere-Düzce Segment with a non-DC content of 18 and 14 per cent, respectively. These values are still within or close to the error bounds derived in Stierle *et al.* (2014). Therefore, we conclude that these events might be even pure shear and the non-DC components are negligible. This correlates well with the predominant strike-slip stress regime along these segments and also with the main shock rupture being right-lateral strike-slip. In contrary, we found a substantial percentage of non-DC components for events below the Akyazi Plain where the Sapanca Fault splits into the Mudurnu and the Karadere faults. The observed non-DC components are entirely positive indicating a tensional regime and ranging from 20 to 48 per cent, clearly exceeding the defined error bounds found in the synthetic study (see Stierle *et al.* 2014). Furthermore it is notable that all tensile events occurred within 4 d approximately

Table 4. Non-DC components of the moment tensors obtained by the inversion constrained to the shear-tensile source model and their stability for the 33 selected events.

ID	DC (per cent)	CLVD (per cent)	ISO (per cent)	Noise σ_{ISO} (per cent)	Noise σ_{CLVD} (per cent)	Jackknife σ_{ISO} (per cent)	Jackknife σ_{CLVD} (per cent)
1	100	0	0	3.3	2.6	3.3	2.6
2	100	0	0	3.9	3.1	2.6	2.0
3	90	4	6	2.7	2.1	2.5	2.0
4	95	2	3	2.6	2.1	2.9	2.3
5	90	4	6	3.3	2.7	3.5	2.8
6	95	−2	−3	4.5	3.6	1.8	1.5
7	100	0	0	4.5	3.6	3.4	2.8
8	100	0	0	4.4	3.5	5.7	4.5
9	95	2	3	6.8	5.4	5.3	4.2
10	74	12	14	5.2	4.1	7.4	5.9
11	71	13	16	6.9	5.5	5.5	4.4
12	74	12	14	8.1	6.5	6.7	5.4
13	68	14	18	6.2	5.0	1.7	1.4
14	78	10	12	5.9	4.8	3.1	2.5
15	57	19	24	5.3	4.3	2.9	2.3
16	74	12	14	2.8	2.2	1.8	1.4
17	59	18	23	2.5	2.0	2.1	1.7
18	65	15	20	2.8	2.3	2.3	1.8
19	68	14	18	7.4	5.9	6.6	5.2
20	78	10	12	3.1	2.5	2.0	1.6
21	74	12	14	1.0	0.8	6.9	5.6
22	82	8	10	8.7	7.0	6.5	5.2
23	78	10	12	3.3	2.6	3.7	2.9
24	52	22	26	2.6	2.1	3.4	2.7
25	78	10	12	3.1	2.5	1.6	1.3
26	100	0	0	3.0	2.4	3.1	2.5
27	95	−2	−3	3.8	3.1	2.7	2.2
28	95	2	3	2.7	2.1	5.1	4.1
29	86	6	8	5.7	4.6	2.0	1.6
30	90	4	6	6.9	5.5	3.4	2.7
31	95	2	3	4.5	3.6	3.6	2.9
32	82	8	10	6.3	5.0	0.9	0.7
33	100	0	0	3.2	2.6	1.4	1.1

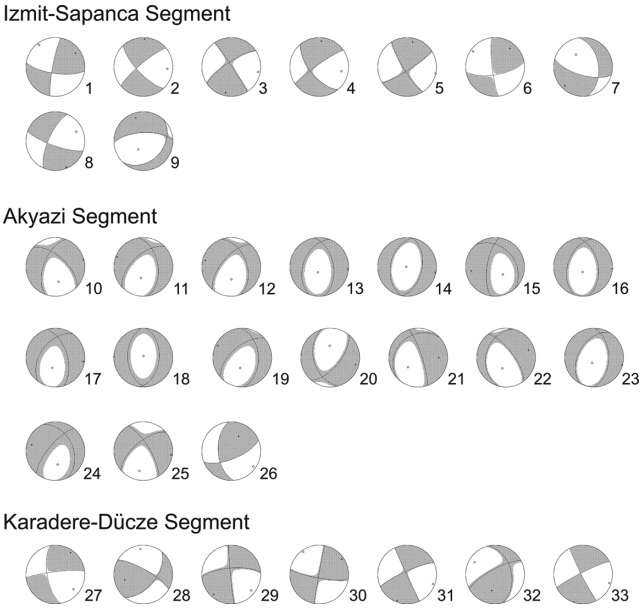

Figure 4. Full moment tensor solutions for the 33 stable events determined using the moment tensor inversion constrained to a shear-tensile source model. The lower hemisphere equal-area projection is used. Compression zones are grey-shaded and red and blue dots indicate resulting *P*- and *T*-axes, respectively.

2 weeks after the main shock, whereas the remaining events occurred 10–57 d after the main shock. Fig. 7 shows a schematic sketch of the tectonic settings along the Akyazi Segment illustrating the interaction of the activated fault segments during the main shock. In this segment, the Sakarya and the Karadere faults slipped during the Izmit main shock with right-lateral motions. However, the observed distribution of surface displacement at the Sakarya Fault decreases linearly from over 5 m in the western part of the branch down to 0–0.1 m at the Akyazi strand (Langridge *et al*. 2002), whereas the observed right-lateral surface displacement at the Karadere Fault is generally much lower being 1–1.5 m and uniformly distributed along the fault. In between, there is a lack of surface displacement over more than 6 km. Consequently, a slip deficit of approximately 3.5 m was generated below the Akyazi Plain coseismically resulting in purely normal faulting aftershock activity with high aftershock energy release and a high potential for tensional source mechanisms. We clearly observe a substantial amount of non-DC components in the seismic moment tensors (Fig. 6) related to tensile fracturing on pre-existing faults. We propose that the high amount of non-DC components is a strong indicator for extensional components in the source mechanism and, therefore, emphasizes the hypothesis of a tensional tectonic setting below the Akyazi Plain during the early post-seismic phase promoting large-scale fluid motion within the crust.

Miller *et al.* (2004) found that large earthquakes can create potential liquid path by hydraulically connecting the upper crust at

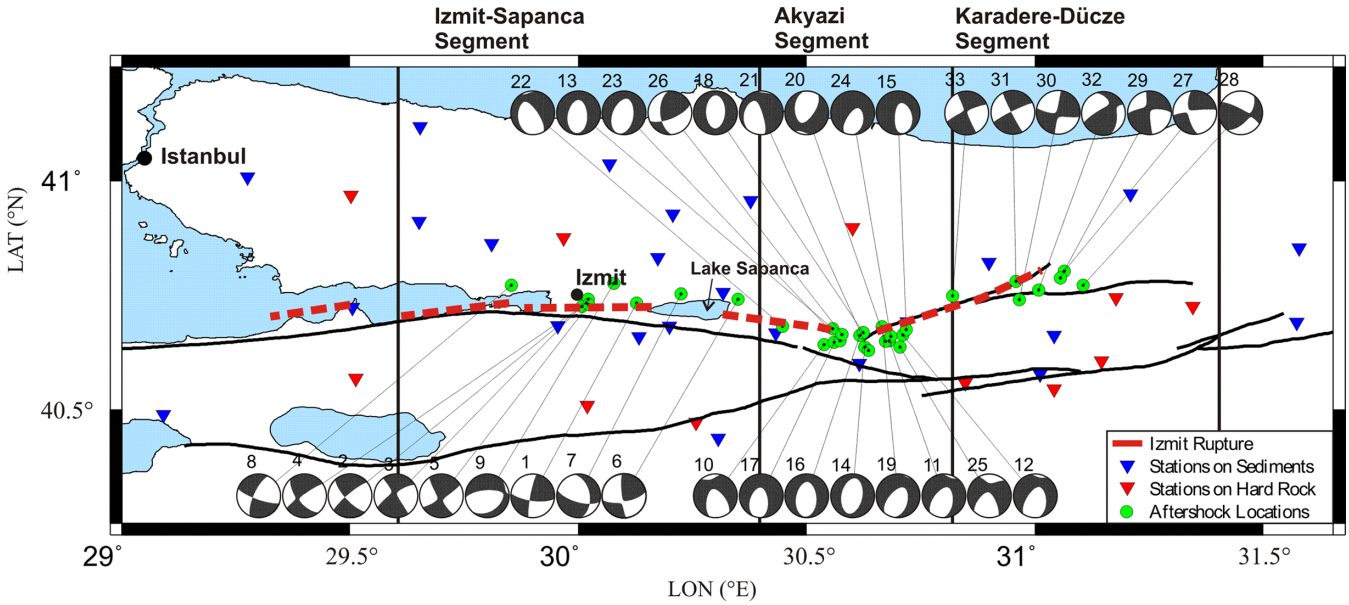

Figure 5. Map view of the lower hemisphere projection of the 33 stable aftershock fault plane solutions. The ID of each event is plotted above the beach ball. Black lines are fault lines taken from the Turkey General Directorate of Mineral Research and Exploration and red lines are surface rupture of the 1999 Izmit earthquake observed by Barka *et al*. (2002).

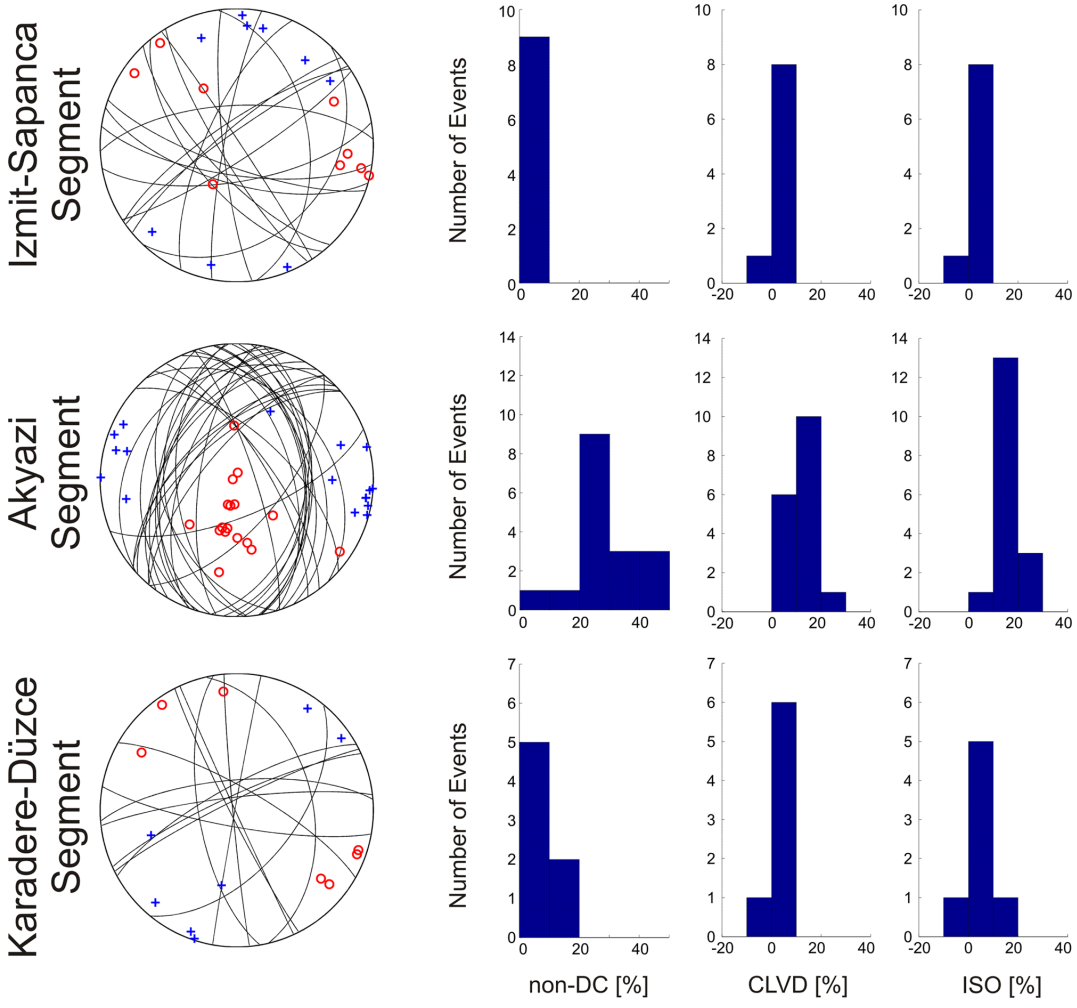

Figure 6. Moment tensors of the 33 selected aftershocks. Left-hand side: nodal lines and *P*- and *T*-axes for events located in the respective segment. Right-hand side: histograms of the non-DC, CLVD and ISO components observed in the corresponding segment.

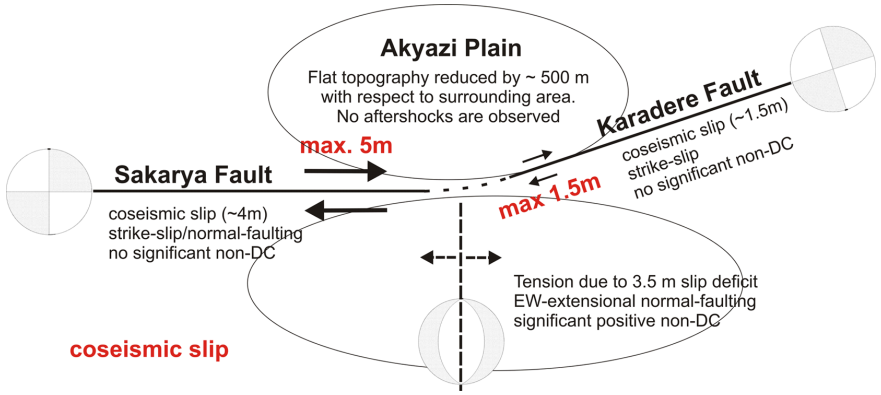

Figure 7. Schematic map view of the Akyazi Segment.

hydrostatic pore pressure with the lower crust at near lithosphere pore pressure. The increased fluid pressure triggered subsequent earthquakes and aftershocks by significantly reducing the effective normal stress on pre-existing faults. The subsequent flow is fast, high-pressured and propagates readily into the new fractures created by the main event thereby promoting tensile fracturing. Thus, this theory may provide a link between the large Izmit earthquakes, its tensile aftershocks and earthquake-triggered large-scale fluid flow. Roux & Ben-Zion (2013) further monitored the fault zone environment of the Düzce event with the correlation of earthquake waveforms. They observed a significant co-main shock change in correlation coefficients of groups of Düzce aftershocks, which indicates interplay between generation and healing of rock damage and permeability in the fault zone combined with a prominent fluid motion. We therefore find our observation of tensile fracturing in an extensional setting such as below the Akyazi Plain after the Izmit earthquake to be another indicator for a large-scale fluid motion in the crust to compensate the accumulated slip deficit.

Interestingly Hearn *et al.* (2009) observed even 2.5 yr after the Izmit main shock a residual component of fault-normal (north–south) extension next to the Akyazi Plain at the Lake Sapanca using post-seismic deformation modelling techniques. They argue that coseismic reduction occurred in effective viscosity of lower crust and upper mantle causing the transfer of background tectonic stress to the upper crust and driving the observed extension on the long-term scale.

4 CONCLUSIONS

We studied potential non-DC components in aftershocks of the 1999 Izmit earthquake. To ensure high-quality data with good focal coverage, we applied strict quality criteria to the aftershock catalogue reducing the number of events from more than 10 000 to only 33 events for which stable moment tensors were obtained. Such a drastic reduction of events would not be necessary if broadband observations of earthquakes were available. While events along the Izmit-Sapanca and Karadere-Düzce segments host mostly strike-slip events with no or insignificant non-DC components, we identified EW-extensional normal faulting events with significant positive non-DC components of up to 48 per cent below the extensional Akyazi Plain. This observation is in accordance with the post-seismic setting following the Izmit main shock that left a remarkable slip deficit of 3.5 m below the Akyazi bend (Fig. 7). We conclude that the tension throughout the seismogenic layer might have allowed fluids to migrate upwards thereby reducing effective normal traction or friction on coseismically stressed normal faults and accelerating the compensation of the slip deficit.

ACKNOWLEDGEMENTS

This work was supported by the German Research Foundation (DFG) under the contract Bo1877/1-1, and by the Grant Agency of the Czech Republic, Grant No. P210/12/1491. We acknowledge funding from the Helmholtz Foundation within the Young Investigator Group ‘From microseismicity to large earthquakes’. We thank the German Task Force for Earthquakes hosted at GeoForschungsZentrum in Potsdam and especially J. Zschau and C. Milkereit for providing the continuous seismic recordings obtained after the 1999 Izmit earthquake. We thank Dino Bindi for discussing and collaborating on attenuation issues. The first author ES thanks the Christiane-Nüsslein-Volhard Foundation for co-funding. We thank the editor Yehuda Ben-Zion and acknowledge comments by Sean Ford and Zacharie Duputel.

REFERENCES

Ambraseys, N.N. & Zatopek, A., 1969. The Mudurnu Valley, West Anatolia, Turkey, earthquake of 22 July 1967, *Bull. seism. Soc. Am.,* **59**(2), 521–589.

Armijo, R., Meyer, B., Navarro, S., King, G. & Barka, A., 2002. Asymmetric slip partitioning in the Sea of Marmara pull-apart: a clue to propagation processes of the North Anatolian Fault? *TerraNova,* **14**(2), 80–86.

Barka, A. *et al.*, 2002. The surface rupture and slip distribution of the 17 August 1999 Izmit earthquake (*M* 7.4), North Anatolian fault, *Bull. seism. Soc. Am.,* **92**(1), 43–60.

Baumbach, M. *et al.*, 2003. Calibration of an ML scale in northwestern Turkey from 1999 Izmit aftershocks, *Bull. seism. Soc. Am.,* **93,** 2289–2295.

Bindi, D., Parolai, S., Grosser, H., Milkereit, C. & Karakisa, S., 2006. Crustal attenuation characteristics in northwestern Turkey in the range from 1 to 10 Hz, *Bull. seism. So. Am.,* **96**(1), 200–214.

Bohnhoff, M., Grosser, H. & Dresen, G., 2006. Strain partitioning and stress rotation at the North Anatolian Fault Zone from aftershock focal mechanisms of the 1999 Izmit $M_w = 7.4$ earthquake, *Geophys. J. Int.,* **166,** 373–385.

Bulut, F., Bohnhoff, M., Aktar, M. & Dresen, G., 2007. Characterization of aftershock-fault plane orientations of the 1999 Izmit (Turkey) earthquake using high-resolution aftershock locations, *Geophys. Res. Lett.,* **34**(20), L20306, doi:10.1029/2007GL031154.

Červený, V., 2001. *Seismic Ray Theory,* Cambridge Univ. Press.

Eken, T., Bohnhoff, M., Bulut, F., Can, B. & Aktar, M., 2013. Crustal anisotropy in the Eastern Sea of Marmara region in northwestern Turkey, *Bull. seism. Soc. Am.,* **103**(2a), doi: 10.1785/0120120156.

Foulger, G.R., Julian, B.R., Hill, D.P., Pitt, A.M., Malin, P.E. & Shalev, E., 2004. Non-double-couple microearthquakes at Long Valley caldera, California, provide evidence for hydraulic fracturing, *J. Volc. Geotherm. Res.,* **132**(1), 45–71.

Görgün, E., Bohnhoff, M., Bulut, F. & Dresen, G., 2010. Seismotectonic setting of the Karadere–Düzce branch of the North Anatolian Fault Zone between the 1999 Izmit and Düzce ruptures from analysis of Izmit aftershock focal mechanisms, *Tectonophysics,* **482**(1), 170–181.

Gülen, L., Pinar, A., Kalafat, D., Ozel, N., Horasan, G., Yilmazer, M. & Isikara, A.M., 2002. Surface fault breaks, aftershock distribution, and rupture process of the 17 August 1999 Izmit, Turkey, earthquake, *Bull. seism. Soc. Am.,* **92**(1), 230–244.

Hearn, E.H., McClusky, S., Ergintav, S. & Reilinger, R.E., 2009. Izmit earthquake postseismic deformation and dynamics of the North Anatolian Fault Zone, *J. Geophys. Res.,* **114,** B08405, doi:10.1029/2008JB006026.

Hurd, O. & Bohnhoff, M., 2012. Stress- and structure-induced shear-wave anisotropy along the 1999 Izmit Rupture, northwest Turkey, *Bull. seism. Soc. Am.,* **102**(5), 2177–2188.

Ickrath, M., Bohnhoff, M., Bulut, F. & Dresen, G., 2013. Stress rotation and recovery in conjunction with the 1999 Izmit M_w 7.4 earthquake, *Geophys. J. Int.,* doi:10.1093/gji/ggt409.

Julian, B.R., Miller, A.D. & Foulger, G.R., 1998. Non-double-couple earthquakes, 1. Theory, *Rev. Geophys.,* **36,** 525–549.

Langridge, R.M., Stenner, H.D., Fumal, T.E., Christofferson, S.A., Rockwell, T.K., Hartleb, R.D., Bachhuber, J. & Barka, A.A., 2002. Geometry, slip distribution, and kinematics of surface rupture on the Sakarya fault segment during the 17 August 1999 Izmit, Turkey, earthquake, *Bull. seism. Soc. Am.,* **92**(1), 107–125.

Miller, A.D., Foulger, G.R. & Julian, B.R., 1998. Non-double-couple earthquakes, 2. Observations, *Rev. Geophys.,* **36,** 551–568.

Miller, S.A., Collettini, C., Chiaraluce, L., Cocco, M., Barchi, M. & Kaus, B.J., 2004. Aftershocks driven by a high-pressure CO2 source at depth, *Nature,* **427**(6976), 724–727.

Örgülü, G. & Aktar, M., 2001. Regional moment tensor inversion for strong aftershocks of the August 17, 1999 Izmit earthquake ($M_w = 7.4$), *Geophys. Res. Lett.,* **28**(2), 371–374.

Parolai, S., Bindi, D., Baumbach, M., Grosser, H., Milkereit, C., Karakisa, S. & Zunbul, S., 2004. Comparison of different site response estimation techniques using aftershocks of the 1999 Izmit earthquake, *Bull. seism. Soc. Am.,* **94**(3), 1096–1108.

Ross, A., Foulger, G.R. & Julian, B.R., 1996. Non-double-couple earthquake mechanisms at the Geysers geothermal area, California, *Geophys. Res. Lett.,* **23**(8), 877–880.

Roux, P. & Ben-Zion, Y., 2013. Monitoring fault zone environments with correlation of earthquake waveforms, *Geophys. J. Int.,* doi:10.1093/gji/ggt441.

Seeber, L., Armbruster, J.G., Ozer, N., Aktar, M., Baris, S., Okaya, D., Ben-Zion, Y. & Field, E., 2000. The 1999 earthquake sequence along the North Anatolia Transform at the juncture between the two main ruptures. In *The 1999 Izmit and Duzce Earthquakes: Preliminary Results,* pp. 209–223, Istanbul Technical University.

Šílený, J., 2009. Resolution of non-double-couple mechanisms: simulation of hypocentre mislocation and velocity structure mismodeling, *Bull. seism. Soc. Am.,* **99,** 2265–2272.

Stierle, E., Vavryčuk, V., Šílený, J. & Bohnhoff, M., 2014. Resolution of non-double-couple components in the seismic moment tensor using regional networks—I: a synthetic case study, *Geophys. J. Int.,* doi:10.1093/gji/ggt502.

Tchalenko, J.S., 1970. Similarities between shear zones of different magnitudes, *Bull. geol. Soc. Am.,* **81**(6), 1625–1640.

Tibi, R. *et al.*, 2001. Rupture processes of the 1999 August 17 Izmit and November 12, Düzce (Turkey) earthquakes, *Geophys. J. Int.,* **144**(2), F1–F7.

Vavryčuk, V., 2001. Inversion for parameters of tensile earthquakes, *J. geophys. Res.,* **106**(16), 16 339–16 355.

Vavryčuk, V., 2002. Non-double-couple earthquakes of January 1997 in West Bohemia, Czech Republic: evidence of tensile faulting, *Geophys. J. Int.,* **149,** 364–373.

Vavryčuk, V., 2005. Focal mechanisms in anisotropic media, *Geophys. J. Int.,* **161,** 334–346.

Vavryčuk, V., 2011. Tensile earthquakes: theory, modeling, and inversion, *J. geophys. Res.,* **116,** B12320, doi:10.1029/2011JB008770.